

**The RITAS algorithm: a constructive yield monitor data processing algorithm for  
soil mapping**

by

**Luis Damiano**

A Creative Component submitted to the graduate faculty  
in partial fulfillment of the requirements for the degree of  
MASTER OF SCIENCE

Major: Statistics

Program of Study Committee:  
Jarad Niemi, Major Professor  
Petruța Caragea  
Bradley Miller

Iowa State University

Ames, Iowa

2020

Copyright © Luis Damiano, 2020. All rights reserved.

## **DEDICATION**

To those who have helped me, those who presently help me, and those who will help me grow.

**TABLE OF CONTENTS**

	Page
LIST OF FIGURES . . . . .	iv
ACKNOWLEDGMENTS . . . . .	v
ABSTRACT . . . . .	vi
1 Introduction . . . . .	1
2 The RITAS algorithm . . . . .	5
3 STRIPS yield mapping . . . . .	11
4 Discussion . . . . .	18
BIBLIOGRAPHY . . . . .	20
APPENDIX . . . . .	24

**LIST OF FIGURES**

	<b>Page</b>
2.1 Close-up illustration of selected algorithm steps . . . . .	5
3.1 Visualization of selected algorithm steps as applied to a specific dataset . .	16
3.2 Visualization of the algorithm output for one field across four different years	17
.1 Step-by-step visualization of the algorithm for one field . . . . .	25

## ACKNOWLEDGMENTS

Funding was provided by Iowa State University through the Presidential Interdisciplinary Research Initiative on C-CHANGE: Science for a Changing Agriculture, and the Foundation for Food and Agriculture Research (FFAR). The dataset used to illustrate our work was collected as part of the Science-Based Trials of Rowcrops Integrated with Prairie Strips (STRIPS) project, which involved the work of the US Fish and Wildlife Service Neal Smith National Wildlife Refuge, numerous technicians and student researchers, and Heartland Cooperative.

## ABSTRACT

Yield monitor datasets are known to contain a high percentage of unreliable records. The current tool set is mostly limited to observation cleaning procedures based on heuristic or empirically-motivated statistical rules for extreme value identification and removal. We propose a constructive algorithm for processing well-documented yield monitor data artifacts without resorting to data deletion. The RITAS algorithm models sample observations as overlapping, unequally-shaped, irregularly-sized, and time-ordered spatial units to better replicate the nature of the destructive sampling process. Smoothing via a Gaussian Process is used to provide map users with spatial-trend visualization. The intermediate steps as well as the algorithm output are illustrated in grain yield maps for an agricultural site.

## 1 Introduction

[Miller et al. \(1988\)](#) were the first to employ geostatistics explicitly in precision agriculture, a discipline that started in 1990 when agriculture shifted from farm-level to site-specific crop management ([Oliver, 2010](#)). Their study, among other things, introduced geostatistics for mapping patterns in soil phosphorus or potassium via interpolation. As defined by the [Council \(1997\)](#), precision agriculture is a data-centered discipline comprising data acquisition at an appropriate scale, data interpretation and analysis, and management response at an appropriate scale and time. The advent of big data has been impacting this field largely, especially in terms of data acquisition, interpretation, and analysis. Computer mapping of yield and soil is one of the main uses of this technology, typically to help customize crop management across and within fields by identifying less productive areas at a sub-field scale ([Lowenberg-DeBoer and Erickson, 2019](#)). Yield data are now recorded automatically for a wide variety of crops including cereal grains, oilseeds, fiber, forage, biomass, fruits and vegetables. These data are known to be accurate at a global scale, yet there exist nuances at a local scale that affect visualization and downstream analysis, and jeopardizes the credibility and validity of management decisions downstream.

[Ross et al. \(2008\)](#) is a synoptic work focused on yield estimation from yield monitor data covering conceptual, modeling, and mechanical aspects. [Arslan and Colvin \(2002\)](#) investigates the impact of yield monitor calibration in yield estimation accuracy. Although not statistical in nature, agronomical studies provide with insight on the physicalities of the system whose sampling process we aim at replicating with our statistical algorithm. Yield monitoring equipment, introduced in the early 1990s, is a set of typically more than six sensors, antennas, and devices attached to combine harvesters that altogether calculate and record grain yield in real time as the machine operator harvests the productive field. At the end of each cycle, which lasts a pre-specified number of seconds

that can be adjusted dynamically by the operator, the monitor logs measurements for more than 15 variables related to geolocation, crop characteristics, and other machine diagnostics.

Numerous works have established that yield datasets contain a high percentage of unreliable data and have proposed cleaning procedures (Blackmore and Marshall, 1996; Moore, 1998; Blackmore, 1999; Thylén et al., 2000; P et al., 2003; Simbahan et al., 2004; Ping and Dobermann, 2005; Sudduth and Drummond, 2007; Sudduth et al., 2012; Mark et al., 2013; Leroux et al., 2018, 2019; Vega et al., 2019). Mechanical measurement errors have been studied in great depth (Arslan and Colvin, 1999, 2002; Grisso et al., 2002; Burks et al., 2004; Hemming and Chaplin, 2005; Fulton et al., 2009; Schuster et al., 2017), yet we could not find model-based data adjustment protocols. Typically, systematic errors are identified using either heuristics or statistical rules with acceptable empirical results but limited probabilistic motivation. With almost unanimous preference for systematic error detection and removal, we have found little development of alternative strategies for error correction or integration such as the one proposed by Bachmaier (2007, 2010); in fact, some methodologies discard as much as one third of the original dataset as summarized by Lyle et al. (2013).

In many cases, these procedures require the map user to set values for tuning parameters such as thresholds. These constants are not learned from the data but set arbitrarily by the user instead, potentially hindering comparisons across users, locations, and years. Moreover, manually-set thresholds become a hurdle in the context of big data: both the amount and the heterogeneity of yield monitor datasets have been increasing as raw data become more abundant and diverse. Additionally, there is a general preference for working with crop yield as the main input of the cleaning procedures. Being a quantity fusing data collected from more than one sensor, each with its own propagating measurement error, it typically has a lower signal-to-noise ratio than the mass random variable. Also, scaling mass to homogenize unequally-sized observational units may potentiate extreme values resulting in a new variable with higher volatility.

Some processing rules, for example those based on the marginal distribution of yield, do not consider the spatial nature of the data. Others collapse all the information in one point on a

2-dimensional plane, thus failing to recognize that the recorded data are in fact associated with overlapping, unequally-shaped, and irregularly-sized aerial units. Each observation is in reality a realization from a continuous spatial stochastic process: time order and spatial superposition are intrinsic characteristics of the destructive sampling scheme worth modeling.

The many variables logged by the yield monitor equipment include harvested mass, geocoordinates, distance traveled, and swath width, which can be used to create an aerial representation of the data. Depending on the hardware, the reported travel distance and speed may be measured by a speed sensor, a GPS receiver, a radar, or a ultrasonic sensor ([Mulla, 2013](#)). When distance is not available, it can be linearly estimated using speed and cycle length or less preferably approximated using the euclidean distance between two subsequent coordinates. The swath width, also known as gathering or cutting width, can be time dependent and the combine's path that may not be correctly reflected in the data logged by the monitor ([Ross et al., 2008](#)). Although equipments provides the operator with tools to adjust the effective width dynamically, in many situations the operator is unable to attend to manual adjustments in real time and thus the logged values simply represents the maximum or theoretical width. We have found three main strategies in the literature combining distance and width to reproduce an approximate spatial representation.

[Blackmore \(1999\)](#) observed that there is a discrepancy between the theoretical and the effective harvested area. One of the reasons is that the recorded header width differs from the width of the header that is truly full of crop at any given time step. While in practice it can be set equal to a fixed proportion of the cutter bar width, e.g. 95%, land finishes and areas close to voids require special treatment as the header could even be empty. In order to avoid any use of the recorded width, and circumvent the uncertainty associated with it, the authors introduced potential mapping. In this technique, the recorded mass of data points belonging to circular neighbourhoods is aggregated and assigned to a new spatial point whose location corresponds to the circle geocenter. The aggregated mass is then spatially re-normalized by the area of the polygons in the Voronoi diagram formed by these new points. This approach has two limitations. First, it transforms data into spatial points and thus incurs in information loss about the shape and size of the observational aerial units (e.g.

different shapes could have the same centroid). Second, an additional gridding technique needs to be applied to analyze temporal trends in yield maps ([Blackmore et al., 2003](#)), effectively displacing the yield measurements twice: all the polygon information is first collapsed into a single point which is displaced afterwards.

Previously, [Han et al. \(1997\)](#) introduced a bitmap approach to determine the actual combine cut width, compute the effective area size, and approximate the new centroid of each spatial unit after removing the area covered by previous observations. To track the covered area at each time step, the author superposes a regular grid where each cell functions as a bitmask indicating whether the pixel has been harvested before or not, hence the name of the methodology. The article does not show how this methodology performs in the presence of sharp turns, where overlaps tend to be larger during the pivoting motion, as these seem to have been removed from the analysis. It is worth noting that, even after processing, the intermediate spatial representations have some overlap and skips left unexplained by the author. Again, as these intermediate spatial representations are collapsed into spatial points, some information is lost. Furthermore, these new data points may not be spatially aligned if temporal analysis was pursued next. Finally, the authors warn that the bitmap initialization process is more complicated when there exists non-crop features such as rivers, canals, or roadways.

Expanding on the bitmap concept, [Drummond et al. \(1999\)](#) developed a method where observational units are represented by polygons constructed from position and trajectory information. These are processed in chronological harvest order by Boolean subtraction to compute the actual harvested area during each time step, effectively retaining full information about the aerial units. As drawbacks, the authors mention the potential overestimation at the boundaries as well as the computational complexity of the algorithm. In the general case, its complexity is order  $O(N^2)$ , yet several strategies for specific cases are discussed there.

## 2 The RITAS algorithm

Our algorithm constructs yield maps through the following steps: Rectangle creation, Intersection assignment, Tessellation, Apportioning, and Smoothing (RITAS). The overarching goal of this process is to mimic the real world harvesting processes. Figure 2.1 provides an illustration of these steps.

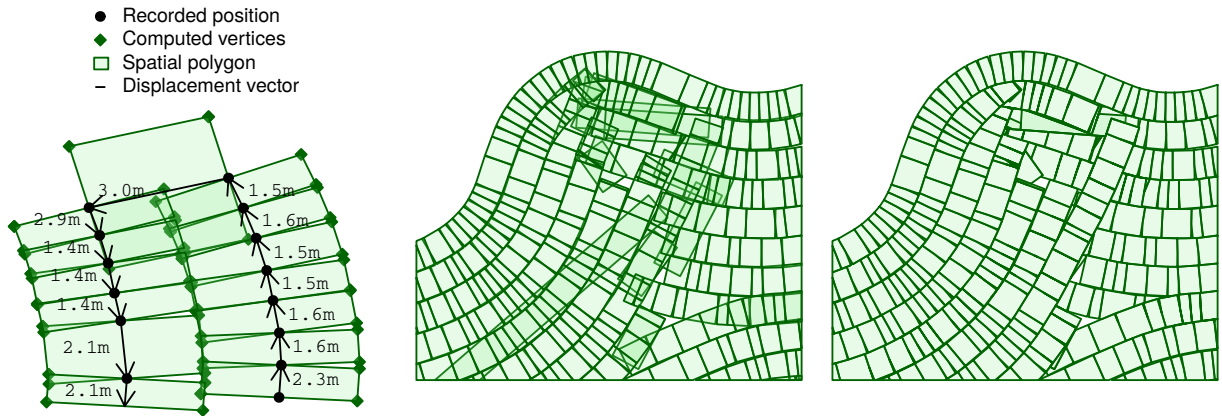


Figure 2.1 Close-up illustration of selected processing steps. Left: Construction of the vehicle polygons from the GPS location data. Black dots mark the location at the end of each logging cycle, green dots correspond to the vertices computed according to the displacement vector implied by two consecutive spatial points. The distance traveled could be reported by the yield monitor or estimated from the vector length. Center: Spatial polygons reveal overlap (darker areas) due to driving maneuvers. Right: Tessellation eliminates the overlap by assigning intersecting areas to the first polygon in time.

Each precision yield data set is assumed to have time-ordered rows containing the following information: mass harvested  $m_t$ , 2-dimensional spatial coordinate  $(x_t, y_t)$ , and swath width  $w_t$  (so that  $w_t$  represents the half-width) for  $t = 0, \dots, T$ ,  $T \in \mathbb{N}$ . We assume any lag time has

been effectively pre-processed by appropriately matching the mass harvested to its 2-dimensional location.

**Step 1: Rectangle creation** Figure 2.1 (left) illustrates the construction of a rectangular polygon representing the harvested area between each sequential pair of spatial coordinates. The position vector  $\mathbf{s}_t = (x_t, y_t)$  represents the location of the tracked device in a 2-dimensional plane at the time step  $t$ , which we assume to be the midpoint of the combine harvester head. The rectangle is then uniquely identified by the position of its four vertices, two representing the beginning of the harvested area at time step  $t - 1$  and two representing the end of the harvested area at time step  $t$ . The linear displacement vector is equal to the vector difference between the position vectors at two subsequent time steps  $\mathbf{s}_t - \mathbf{s}_{t-1}$ . The first two vertices are computed as the endpoints of a line segment perpendicular to the displacement vector with midpoint at  $\mathbf{s}_{t-1}$  and length equal to the swath width. The remaining two vertices are found using the same procedure but pivoting on the midpoint  $\mathbf{s}_t$  instead. Given a pair of position vectors  $\mathbf{s}_t, \mathbf{s}_{t-1}$ , denote  $b_t = (y_t - y_{t-1})/(x_t - x_{t-1})$  the slope of the connecting line, and define  $dx_t = 0.5w_t(1 + b_t^{-2})^{-\frac{1}{2}}$  and  $dy_t = -dx_t b_t^{-1}$ . Then, the rectangle associated with mass  $m_t$  has the four vertices coordinates given by  $\{(x_i \pm dx_t, y_i \pm dy_t) : i = t, t - 1\}$ . As the first spatial point has no displacement, this processing yields  $T$  rectangles with vertices collected in the set  $\mathcal{P} = \{P_\tau : \tau \in \{1, \dots, T\}\}$ . Note that the measurement unit of the header width, typically reported in meters or feet, and the coordinate reference system should be homogenized appropriately.

**Step 2: Intersection assignment** Geometries in  $\mathcal{P}$  represent the area over which the combine harvester passed, which may differ from the effectively harvested area at each time step. Yield monitors allow the operator to dynamically record the proportion of the header being full of crop, yet the operator may not make adjustments consistently and accurately. More expensive gear includes sensing equipment for assessing crop width automatically. The header may not be full of crop when harvesting the field boundaries (e.g. on outer edges, around voids), or within them. The first pattern can be identified by visual inspection as long strips of indicated low yield running

along the length of the field [Blackmore \(1999\)](#). Several algorithms for this first kind of harvesting dynamics, which is beyond the scope of our algorithm, have been proposed.

In the second case, as a byproduct of the destructive sampling scheme, the discrepancy is linked to the spatial superposition of the observational units that arise due to local harvesting dynamics such as turns, wedges, parallel lines, and traveling over harvested areas. Globally within a field, this phenomenon can be exacerbated by factors such as field characteristics, or narrow row crops (e.g. wheat). Generally, overlapping cannot be assumed symmetrical nor time-invariant. For example, pivoting motions overlap on the inner side and the proportion of duplicated area varies at each time step depending on factors such as the sharpness of the turns, the angle of the wedges, or the obstacles faced by the operator.

As a general framework to model the time-varying effectively harvested area, we run a time-ordered apportioning procedure over the rectangles in  $\mathcal{P}$ . Let  $\tilde{P}_\tau = P_t \setminus \left( \bigcup_{i=1}^{t-1} P_i \right)$  be the time-ordered relative complement of the previously harvested area in the rectangle corresponding to the time step  $t$ . By doing this, we effectively map the set of overlapping rectangles  $\mathcal{P}$  into a set of non-overlapping polygons  $\tilde{\mathcal{P}} = \{\tilde{P}_\tau : \tau \in \{1, \dots, T\}\}$ . When the original dataset has no voids (e.g. unplanted, flooded, or more generally inaccessible sub areas),  $\tilde{\mathcal{P}}$  form a flat plane covered by tiles with no overlaps and no gaps (non-periodic tessellation). Some of the computational considerations discussed in [Drummond et al. \(1999\)](#) are relevant for implementing this step.

Figure 2.1 (middle) shows end result of this construction which produces rectangles that overlap, an area called the *intersection*, due to adjacent harvester paths. Figure 2.1 (right) shows the resulting tiled plane. This step creates  $T$  polygons partitioning the harvested area, each associated with the same mass it had in Step 1 but now the area may be smaller (due to the intersection removal) and thus yield is more accurately captured.

**Step 3: Tessellation and Apportioning** The elements in  $\tilde{\mathcal{P}}$  are unsuitable for spatial techniques that do not accomodate to areas with irregular shapes and heterogeneous area sizes. Two equally-sized long rectangles, one in a vertical and the other in a horizontal position, would have the same centroid yet they convey different information about yield to the north or west of the

centroids. Alternatively, two centered equally-shaped polygons with different sizes carry different information about the spatial coverage of the collected data. To normalize the aerial representation in terms of both shape and size, we superimpose a regular grid of square pixels, assign portions of the polygons into grid pixels, and apportion the harvested mass associated with the polygons to the pixels. The first two steps involve topology operations on geometries whereas the last one involves manipulation of the numerical data. Accounting for these two spatial features is by itself a methodological improvement over the surveyed algorithms, which simply reduce data to spatial points such as the displacement vector endpoint or, less commonly, the polygon centroid.

Let  $\mathcal{P}_N^*$  be a set of  $N \in \mathbb{N}$  equally-sized, non-overlapping, and contiguous squared pixels forming a grid covering all the elements in  $\tilde{\mathcal{P}}$ . The constant  $N$  reflects the preference of the map user in terms of resolution, selected either by the total number of pixels, more intuitively by the pixel length in meters, or the target computational time investment. Although pixels size can be set arbitrarily, its choice should consider the accuracy of the position system. We take the pairwise intersection among the elements in  $\tilde{\mathcal{P}}$  and  $\mathcal{P}_N^*$  and compute  $\pi_{\tau,n} \in [0, 1]$  the proportion of the area in the  $\tau$ -th non-overlapping polygon  $P_\tau$  that intersects with the  $n$ -th pixel in the grid for  $\tau \in \{2, \dots, T\}$  and  $n \in \{1, \dots, N\}$ . The corresponding proportion of the harvested mass  $m_\tau$  associated with  $P_\tau$  is assigned to  $P_N^*$ . The total harvested mass associated with the  $n$ -th pixel is given by  $m_n^* = \sum_{\tau=2}^T \pi_{\tau,n} m_\tau$ . The resulting polygons in  $\mathcal{P}_N^*$  resemble much the Basic Areal Units (BAUs) as defined by [Nguyen et al. \(2012\)](#) in the context of massive data fusion: fine-scale, nonoverlapping, aerial regions representing the smallest resolution at which data is aggregated.

Two key aspects behind the gridding strategy are worth mentioning. First, for the purpose of apportioning, we assume that the harvested mass associated with the spatial polygons is distributed uniformly within each unit. This is a sensible assumption in this context as combine harvester log data in short cycles and the spatial polygons represent small areas for the scale of the underlying crop growth process.

Second, if one imposes regularity and equal-shape conditions on the grid elements and also forces it to cover all the elements in  $\tilde{\mathcal{P}}_\tau$ , the sum of the pixels area may exceed the sum of the

tessellated polygons area. The excess, found at both the harvested region outer borders and the inner voids boundaries, can be diagnosed visually with ease. It decreases as the grid resolution, or equivalent as the total number of pixels  $N$ , increases and so can be controlled at the cost of additional computational time for topology operations and smoothing. Concretely, when a Gaussian Process is applied for smoothing as described below, exact inference has time complexity in the order of  $O(N^3)$  and storage demands of  $O(N^2)$ . In other words, as we double the map resolution, we octuple the number of operations and quadruple the need for storage. Alternatively, one could exclude the pixels with less than an arbitrary proportion of area effectively covered by the tessellated observations. A sensible choice, such as a minimum coverage of 50%, will tend to balance under and over-covered polygons. Due care should be taken so that apportioning is still applied validly: mass should be allocated to pixels only in proportion of the actual overlapping area, discarding any part of the tessellated polygons that is not covered by any pixel. Note that the grid resolution serves only for the purpose of spatial aggregation, and need not be the same resolution used for the visualization that will be introduced in the following step.

Mass is apportioned from the polygons of Step 2 to tiles in the grid according to their proportion of the total polygon area. Where tiles overlap multiple polygons, the tiles receive mass from each of the polygons according to the area of overlap relative to each polygon's area. Thus, the mass associated with the  $n$ th tile is  $m_n^* = \sum_{t=1}^T p_{t,n} m_t$  where  $p_{t,n}$  is the proportion of polygon  $t$ 's area in the intersection of polygon  $t$  and tile  $n$ . This step creates  $N$  polygons, determined by the user based on tessellation resolution, partitioning the harvested area each with an associated mass of harvested crop. Figure 3.1 (bottom left) shows the regular grid with apportioned mass. The regular tessellation provides constant areas and meaningful centroids, and therefore we can use standard spatial smoothing techniques directly on mass, as opposed to yield.

**Step 4: Smoothing** McCullagh and Clifford (2006) provided empirical evidence suggesting that the non-anthropogenic spatial variation in yield, defined as patterns that cannot be explained by topography or human intervention, matches the characteristics of the de Wijs process plus white noise. We smooth using a Gaussian Process (GP) with a Matérn covariance on the logarithm of

mass (Handcock and Stein, 1993; Guttorp and Gneiting, 2006), which becomes similar to a Wijs process as the length scale tends to zero. Compared with the more common powered exponential covariance functions, e.g. Gaussian or exponential, the Matérn adds an additional parameter that controls local smoothness, i.e. differentiability, and therefore is often more accurate for real world processes.

Covariance parameters are estimated, and smoothed values are found for each tile following Cressie (1993). Specifically, for each tile we have a predicted mean  $\hat{\mu}_\ell$  and variance  $\hat{\sigma}_\ell^2$  for the logarithm of mass. We use the following formulas to convert back to the mean and variance of mass

$$\hat{\mu}_m = \exp(\hat{\mu}_\ell + \hat{\sigma}_\ell^2/2), \quad \text{and} \quad \hat{\sigma}_m^2 = \exp(2\hat{\mu}_\ell + \hat{\sigma}_\ell^2) [\exp(\hat{\sigma}_\ell^2) - 1].$$

Finally, yield is calculated by dividing the tile mass by the tile area.

### 3 STRIPS yield mapping

In this section, we illustrate the functioning and the results of our methodology when applied to yield monitor data collected from the same agricultural site over the years. We start with a detailed discussion of the production of the yield map for one specific year, and we finally show some resulting visualizations for the same fields but different crops and years.

The data arises from a study conducted at the Neal Smith National Wildlife Refuge in central Iowa to quantify the impact of grassland-to-cropland conversion on nitrate-nitrogen ( $\text{NO}_3\text{-N}$ ) concentrations in soil and shallow groundwater and to assess the potential for perennial filter strips to mitigate increases in  $\text{NO}_3\text{-N}$  levels ([Zhou et al., 2010](#)). The experiment was run in different study sites within the 3000-ha area managed by the U.S. National Fish and Wildlife Service, located in the Walnut Creek watershed in Jasper County, Iowa. In this case study, we focus on one specific site named Basswood that is situated west to the Basswood Trailhead.

Basswood, located at WGS84 15 N 0477097E 4598644N, has a total area of approximately 13 Ha. Nearly 81% of the surface is cropland; most of the remaining proportion is reconstructed prairie vegetation planted as part of the experimental design. For the purpose of our yield maps, these areas are treated as voids because no data were collected from that surface. Cropland in the experiment is in a maize–soybean rotation using standard no-till soil and weed-management techniques. Geographic coordinates, sample time, moisture content, and maize (2008, 2010, 2012, 2014) and soybean (2009, 2011, 2013, 2015) flow rate were reported by a Case IH AFS Pro-600 combine-mounted yield monitor every 1-3 s during crop harvest, resulting in a fine-scale spatially referenced dataset of crop yields across the study area. [Schulte et al. \(2017\)](#) provides a detailed account of the experiment protocol and the resulting improvements in the biodiversity and the delivery of multiple ecosystem services.

The yield monitor dataset for the year 2012 has 4,239 observations logged each three seconds starting from the southwest corner of the site. The swath width was reported to be constant at 6.10 m as the operator did not adjust the proportion of cut head while driving. The distance traveled during each cycle, with an overall mean of 3.7 m, has three modes with centers at 1.9, 4.0, and 6.0 m. The distribution of the yield reported by the monitor, with its median located at 6.3 mg/ha and the 90% of observations being within 1.4 and 10.8 mg/ha, is symmetric and platykurtic. Visual inspection suggests that there are approximately 20 extreme values on the right tail. Small areas within the field boundaries without data, visualized as voids in the maps, correspond to small portions of soil allocated for nonproductive purposes (e.g. perennial crops, research equipment).

Figure 3.1 (top left) displays the simplest form of a yield map. Data points are visualized as equally-sized symbols with colors indicating the yield level at each location. A single-hue shade of green is chosen to ease the interpretation with dark shades being intuitively associated with relatively higher crop yield. The characteristics of the yield distribution vary largely across sites, crop types, and years. Since the main objective of yield map analysis is to identify sub-field areas with different performance levels, the points are colored according to a measure of relative yield within the dataset as opposed to an absolute scale. As a general rule, we define the color gradient as a function of the empirical quartiles in order to guarantee that low and high yield measurements are uniformly represented at the same time that the interpretation guidelines remain consistent across maps.

The proposed coloring scheme helps capturing the large-scale spatial trends: the east area, both above and below the perennial crop strip, and the northwest area show the best relative performance whereas the southwest borderline is underperforming. Another evident pattern is outer borders and borders around inner voids displaying lower yield, which could be explained by soil fertility properties or could simply be a byproduct of how data is collected. Data artifacts due to narrow finishes are well documented: if the header cut was not full when harvesting the boundaries and the operator failed to manually flag it, yield would be underestimated. Careful consideration should be given to neighbouring points that are not on the borders. Light green

points on the northern borderline are adjacent to dark green points, suggesting that this might very well be an artifact due to deficiencies in the the data collection procedure. On the other hand, data points on the southwest zones are consistently underperforming, thus suggesting the existence of an actual spatial trend.

Using points to visualize the data provides no information about the shape of the aerial observational unit and hides the overlaps in the harvested areas, which should be considered appropriately when computing the estimated yield at a given spatial location. In fact, from the figure it is not evident that there is 9.0% of aerial overlap, defined as the percent excess of the sum of the individual rectangles area over the polygons union area.

We apply the RITAS algorithm. Figure .1 (top right), displaying the constructed spatial polygons, makes overlapping patterns more evident: (i) subsequent samples overlap during turns, especially on the inner side; (ii) near voids, where the landscape requires more maneuvering; (iii) wedges formed by perpendicular passing, for example on the western part of the field; (iv) driving from one part to another; (v) between parallel passings and narrow segments.

Because overlapping produces a systematic overestimation of the effective area size, thus biasing down the estimated yield, its correct treatment can uncover performing areas. In all these cases, the coloring suggests that highly overlapping polygons are associated with lower yields. We note, however, that yield was computed using the theoretical polygon area which overestimates the effective harvest area. In Figure .1 (middle left), which shows the reshaped polygons and the yield computed with the new effective area, we notice that some of the sub field areas with low-yield polygons now display a better performance suggesting that this visual artifact was indeed caused by the overlapping. As a computational note, when producing the reshaped polygons, 10 spatial polygons whose area had been fully harvested in previous time steps were dropped from the dataset causing an minor leakage of 0.1% of the total harvest mass; in case of major situations, aggregating the mass of fully nested geometries would be appropriate.

As the ultimate goal of the visualization work is to support the map user's decision making process, the clipped map is not adequate. Crop management decisions at a sub-field scale are

based on spatial trends whereas the measurements are highly noisy due to a combination of at least 10 possible types of data collection error as discussed in [Lyle et al. \(2013\)](#). For example, in Figure [.1](#) there are zones of predominating high and low yield contaminated with scattered observations with the opposite color, and there are also zones with a combination where it is difficult to identify local trends.

Smoothing is thus typically applied. As discussed in the previous section, off-the-shelf smoothing techniques are not suitable for unequally-sized polygons. We superimpose a grid with 4,194 squares at a 5-meter resolution and apportion the harvested mass of the reshaped polygons into the corresponding pixels. As we retain those pixels with at least 50% of their area covered by observations only, we find local zones with under or over coverage. Overall, the whole grid covers 2.6% less of the sampled surface, a discrepancy that can be diminished by increasing the grid resolution.

The results are seen in Figure [3.1](#) (bottom right). The effect of smoothing on the signal to noise ratio is evident from the figure. The richness of smoothing is not only on the visualization, but also on the interpretation of the estimated parameters. We then propose that yield maps should not only include the spatial polygons, but also statistical information useful for the map user. The range, for instance, is informative for map users to better understand the scale of the spatial effect and adjust the scale of their decisions accordingly.

The smooth map is consistent with the main spatial trends observed so far. Clear patterns become more evident now; in the mixed areas, smoothing helps not only to identify the overall local trend but also to make internal breaks/borders more visible. Additional features can help with interpretation include contour lines, e.g. each 1 mg/ha similar to [Blackmore \(1999\)](#), or color schemes based on spatial clusters.

We have implemented our algorithm in the R programming language, using the R packages doParallel, foreach, gstat, rgeos, and sp ([Pebesma, 2004](#); [Pebesma and Bivand, 2005](#); [Bivand et al., 2013](#); [Gräler et al., 2016](#); [Microsoft and Weston, 2017](#); [Corporation and Weston, 2018](#); [R Core Team, 2019](#); [Bivand and Rundel, 2019](#)).

When doing exact inference for a Gaussian Process, smoothing requires the inversion of a square matrix with size equal to the number of observations in the aggregation step, which in this case study is 3,738 pixels. Unless resorting to approximate interpolation methods, significant time is expected to be consumed for this purpose. As a palliative, our implementation optionally divides the prediction space into smaller subsets to be computed in parallel. Although there is no direct gain in the matrix inversion time, it provides some marginal improvements as our prediction space is large with more than 90,000 pixels.

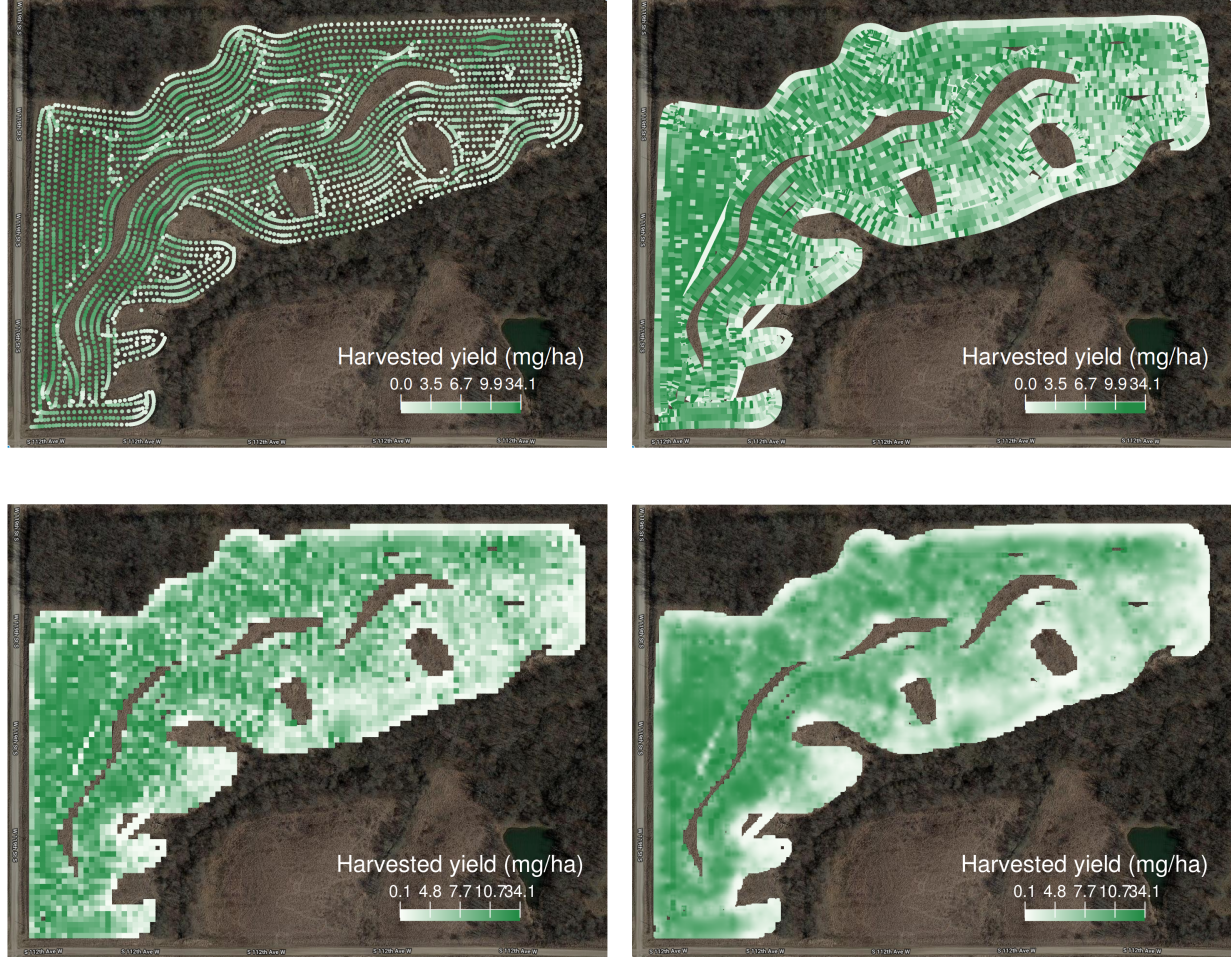


Figure 3.1 Visualization of selected intermediate steps involved in the algorithm for the harvested grain yield of Basswood on year 2012 (maize). Top left: Point map where each observation is marked with equally-sized points placed at the each logging location. Information relevant to spatial trends are hard to observe, such as area coverage and overlaps. Top right: Map of the clipped polygons. Highly intertiment coloring in noisy areas hinder the visualization of the spatial trends, hence the need for smoothing. Bottom left: Map of the aggregated grid at a 5 m resolution. This step produces equally-sized, regularly-shaped polygons suitable for spatial interpolation. Bottom right: Map to be shown to the user. By increasing color homogeneity at a local level, low and high yield areas have a larger contrast and become easier to identify.

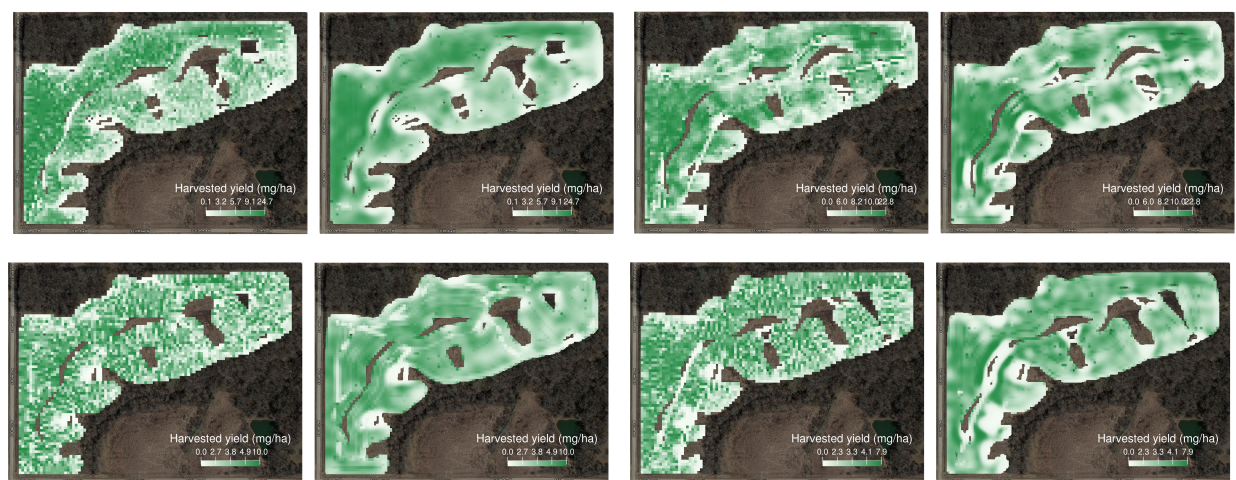


Figure 3.2 Visualization of the harvested grain yield for Basswood in four different years. Maize in the top row, soybean in the bottom row. Aggregated yield in odd columns, smoothed yield in even columns. Although soybean data shows larger variability, as clearly displayed on the aggregated grid, the smooth map offer a clear visualization of the spatial trends.

## 4 Discussion

We have proposed an algorithm for data processing and visualization that is designed for situations where the destructive sampling scheme incorporates other non-trivial features, namely time order and unequally-sized, irregularly-shaped, and possibly overlapping aerial observational units. Reproducing the sampling process, the rules unpack the georeferenced coordinates, recorded as points in a 2-dimensional space, into polygons that are next tiled. The resulting geometries are aggregated using basic aerial units and apportioned assuming that the variable of interest follows a uniform distribution at the local scale. The final output of the processing rules is in the form of many equally sized and shaped polygons, or pixels, equipped with both their associated observed and smoothed yield; the output is meant for both data analysis and visualization. As a byproduct, because the location of the pixels in both the aggregation and smoothing grids can be chosen freely without affecting the validity of the algorithm, spatial registration of the output is readily available.

To illustrate the main characteristics of our procedure, we have presented a case study of grain yield data processing and visualization. Whereas the previous work in precision agriculture presents an almost unanimous preference for extreme values detection and removal, with up to 32% of the data excluded [Lyle et al. \(2013\)](#), our physically principled approach generates a smooth visualization while retaining as much information as collected. This improvement is partly explained by our reproducing of the sampling scheme, but also by a twist how the problem has been traditionally framed: recognizing that local yield is a highly volatile measurement unit due to scaling and error propagation, and thus effectively shifting the baseline variable from yield to mass. Also in contrast with previously proposed methodologies, most of which require the map producer to set arbitrary thresholds, our algorithm is autonomous. There are two main advantages associated with this: (i) large amount of grain yield datasets can be processed automatically, a relevant feature in the

current times where data collection has became accessible and widespread even at a small farming scale; and (ii) the final outputs become more consistent across different users, fields, and years.

Future improvements of this algorithm could come from three perspectives: assumptions, visualization, and computations. One of the main assumptions is that, at a local scale, the random variable of interest follows a uniform distribution. Although this is a reasonable idealization for the case study given the small area of the observational units relative to the rate of change of the underlying process, applications for highly-distanced observations or rapidly-changing underlying processes may require the extension to a different distribution (e.g. exponential decay from the centroids of the polygons to its boundaries). The yield monitor records additional variables that are currently not exploited by our algorithm, which could be enhanced for example by smoothing via universal kriging with automatic relevance determination for feature selection.

To improve visualizations, the smooth map could profit from better display techniques to signal the contrast between low and high valued areas (e.g. contour lines, spatial clustering techniques). In the specific case of grain yield maps, we still observe that some of the well-known sources of yield data error transpire through the algorithm. Some of these can be treated previously to running the algorithm, for example the time lag effect, the harvester fill mode error, and position errors as described in [Blackmore \(1999\)](#).

On the computational side, the case study suggests that the most time insuming steps are smoothing and tiling, respectively. The former could be reduced by resourcing to approximation methods for Gaussian Process spatial interpolation ([Shi and Cressie, 2007](#); [Cressie and Johannesson, 2008](#); [Katzfuss and Cressie, 2011](#); [Nguyen et al., 2012, 2014](#)), approximate linear algebra routines, or a more efficient interpolation technique. Although the intrinsic sequential nature of the sampling scheme limits the potential of parallelization in the tiling step, some performance improvements could be potentially achieved by subdividing the spatial domain into disjoint blocks that should after be accordingly recoupled (divide and conquer). Alternatively, the bitmap matrix of [Han et al. \(1997\)](#) could be revisited as an approximation to our polygon approach. These gains could turn the current work into a near real-time algorithm.

## BIBLIOGRAPHY

- Arslan, S. and Colvin, T. S. (1999). LABORATORY PERFORMANCE OF a YIELD MONITOR. *Applied Engineering in Agriculture*, 15(3):189–195.
- Arslan, S. and Colvin, T. S. (2002). Grain yield mapping: Yield sensing, yield reconstruction, and errors. *Precision Agriculture*, 3(2):135–154.
- Bachmaier, M. (2007). Using a robust variogram to find an adequate butterfly neighborhood size for one-step yield mapping using robust fitting paraboloid cones. *Precision Agriculture*, 8(1-2):75–93.
- Bachmaier, M. (2010). A yield mapping procedure based on robust fitting paraboloid cones on moving elliptical neighborhoods and the determination of their size using a robust variogram. *Positioning*, 01(01):27–41.
- Bivand, R. and Rundel, C. (2019). *rgeos: Interface to Geometry Engine - Open Source ('GEOS')*. R package version 0.4-3.
- Bivand, R. S., Pebesma, E., and Gomez-Rubio, V. (2013). *Applied spatial data analysis with R, Second edition*. Springer, NY.
- Blackmore, B. S. and Marshall, C. J. (1996). Yield mapping: Errors and algorithms. In *ACSESS publications*. American Society of Agronomy, Crop Science Society of America, Soil Science Society of America.
- Blackmore, S. (1999). Remedial correction of yield map data. *Precision Agriculture*, 1(1):53–66.
- Blackmore, S., Godwin, R. J., and Fountas, S. (2003). The analysis of spatial and temporal trends in yield map data over six years. *Biosystems Engineering*, 84(4):455–466.
- Burks, T. F., Shearer, S. A., Fulton, J. P., and Sobolik, C. J. (2004). EFFECTS OF TIME-VARYING INFLOW RATES ON COMBINE YIELD MONITOR ACCURACY. *Applied Engineering in Agriculture*, 20(3):269–275.
- Corporation, M. and Weston, S. (2018). *doParallel: Foreach Parallel Adaptor for the 'parallel' Package*. R package version 1.0.14.
- Council, N. R. (1997). *Precision Agriculture in the 21st Century*. National Academies Press.
- Cressie, N. and Johannesson, G. (2008). Fixed rank kriging for very large spatial data sets. *Journal of the Royal Statistical Society: Series B (Statistical Methodology)*, 70(1):209–226.

- Cressie, N. A. C. (1993). *Statistics for Spatial Data*. John Wiley & Sons, Inc.
- Drummond, S. T., Fraisse, C. W., and Sudduth, K. A. (1999). COMBINE HARVEST AREA DETERMINATION BY VECTOR PROCESSING OF GPS POSITION DATA. *Transactions of the ASAE*, 42(5):1221–1228.
- Fulton, J. P., Sobolik, C. J., Shearer, S. A., Higgins, S. F., and Burks, T. F. (2009). Grain yield monitor flow sensor accuracy for simulated varying field slopes. *Applied Engineering in Agriculture*, 25(1):15–21.
- Gräler, B., Pebesma, E., and Heuvelink, G. (2016). Spatio-temporal interpolation using gstat. *The R Journal*, 8:204–218.
- Grisso, R. D., Jasa, P. J., Schroeder, M. A., and Wilcox, J. C. (2002). YIELD MONITOR ACCURACY: SUCCESSFUL FARMING MAGAZINE CASE STUDY. *Applied Engineering in Agriculture*, 18(2).
- Guttorp, P. and Gneiting, T. (2006). Studies in the history of probability and statistics XLIX On the Matérn correlation family. *Biometrika*, 93(4):989–995.
- Han, S., Schneider, S. M., Rawlins, S. L., and Evans, R. G. (1997). A BITMAP METHOD FOR DETERMINING EFFECTIVE COMBINE CUT WIDTH IN YIELD MAPPING. *Transactions of the ASAE*, 40(2):485–490.
- Handcock, M. S. and Stein, M. L. (1993). A bayesian analysis of kriging. *Technometrics*, 35(4):403–410.
- Hemming, N. and Chaplin, J. (2005). DETERMINING LAG TIME FOR MASS FLOW IN a COMBINE HARVESTER. *Transactions of the ASAE*, 48(2):823–829.
- Katzfuss, M. and Cressie, N. (2011). Spatio-temporal smoothing and EM estimation for massive remote-sensing data sets. *Journal of Time Series Analysis*, 32(4):430–446.
- Leroux, C., Jones, H., Clenet, A., Dreux, B., Becu, M., and Tisseyre, B. (2018). A general method to filter out defective spatial observations from yield mapping datasets. *Precision Agriculture*, 19(5):789–808.
- Leroux, C., Jones, H., Clenet, A., and Tisseyre, B. (2019). Knowledge discovery and unsupervised detection of within-field yield defective observations. *Computers and Electronics in Agriculture*, 156:645–659.
- Lowenberg-DeBoer, J. and Erickson, B. (2019). Setting the record straight on precision agriculture adoption. *Agronomy Journal*, 111(4):1552.

- Lyle, G., Bryan, B. A., and Ostendorf, B. (2013). Post-processing methods to eliminate erroneous grain yield measurements: review and directions for future development. *Precision Agriculture*, 15(4):377–402.
- Mark, S., Adriano, A., and Jose, M. (2013). A simple method for filtering spatial data. In *Precision agriculture'13* (pp. 259–266).
- McCullagh, P. and Clifford, D. (2006). Evidence for conformal invariance of crop yields. *Proceedings of the Royal Society A: Mathematical, Physical and Engineering Sciences*, 462(2071):2119–2143.
- Microsoft and Weston, S. (2017). *foreach: Provides Foreach Looping Construct for R*. R package version 1.4.4.
- Miller, M. P., Singer, M. J., and Nielsen, D. R. (1988). Spatial variability of wheat yield and soil properties on complex hills. *Soil Science Society of America Journal*, 52(4):1133.
- Moore, M. (1998). *An investigation into the accuracy of yield maps and their subsequent use in crop management*. phdthesis, Cranfield University, Silsoe College.
- Mulla, D. J. (2013). Twenty five years of remote sensing in precision agriculture: Key advances and remaining knowledge gaps. *Biosystems Engineering*, 114(4):358–371.
- Nguyen, H., Cressie, N., and Braverman, A. (2012). Spatial statistical data fusion for remote sensing applications. *Journal of the American Statistical Association*, 107(499):1004–1018.
- Nguyen, H., Katzfuss, M., Cressie, N., and Braverman, A. (2014). Spatio-temporal data fusion for very large remote sensing datasets. *Technometrics*, 56(2):174–185.
- Oliver, M., editor (2010). *Geostatistical Applications for Precision Agriculture*. Springer Netherlands.
- P, N., T, M., and M, D. (2003). An algorithm for automatic detection and elimination of defective yield data. In *Precision Agriculture*, 3, pages 445–450. Wageningen Academic Publishers.
- Pebesma, E. J. (2004). Multivariable geostatistics in S: the gstat package. *Computers & Geosciences*, 30:683–691.
- Pebesma, E. J. and Bivand, R. S. (2005). Classes and methods for spatial data in R. *R News*, 5(2):9–13.
- Ping, J. L. and Dobermann, A. (2005). Processing of yield map data. *Precision Agriculture*, 6(2):193–212.
- R Core Team (2019). *R: A Language and Environment for Statistical Computing*. R Foundation for Statistical Computing, Vienna, Austria.

- Ross, K. W., Morris, D. K., and Johannsen, C. J. (2008). A review of intra-field yield estimation from yield monitor data. *Applied Engineering in Agriculture*, 24(3):309–317.
- Schulte, L. A., Niemi, J., Helmers, M. J., Liebman, M., Arbuckle, J. G., James, D. E., Kolka, R. K., O’Neal, M. E., Tomer, M. D., Tyndall, J. C., Asbjornsen, H., Drobney, P., Neal, J., Ryswyk, G. V., and Witte, C. (2017). Prairie strips improve biodiversity and the delivery of multiple ecosystem services from corn–soybean croplands. *Proceedings of the National Academy of Sciences*, 114(42):11247–11252.
- Schuster, J. N., Darr, M. J., and McNaull, R. P. (2017). Performance benchmark of yield monitors for mechanical and environmental influences. In *2017 ASABE Annual International Meeting*, page 1. American Society of Agricultural and Biological Engineers.
- Shi, T. and Cressie, N. (2007). Global statistical analysis of MISR aerosol data: a massive data product from NASA’s terra satellite. *Environmetrics*, 18(7):665–680.
- Simbahan, G. C., Dobermann, A., and Ping, J. L. (2004). Screening yield monitor data improves grain yield maps. *Agronomy Journal*, 96(4):1091.
- Sudduth, K. A. and Drummond, S. T. (2007). Yield editor. *Agronomy Journal*, 99(6):1471.
- Sudduth, K. A., Drummond, S. T., and Myers, D. B. (2012). Yield editor 2.0: Software for automated removal of yield map errors. In *2012 Dallas, Texas, July 29 - August 1, 2012*. American Society of Agricultural and Biological Engineers.
- Thylén, L., Algerbo, P. A., and Giebel, A. (2000). An expert filter removing erroneous yield data. In Robert, P. C., Rust, R. H., and Larson, W. E., editors, *Proceedings of the 5<sup>th</sup> International Conference on Precision Agriculture, Bloomington, Minnesota, USA, 16-19 July, 2000.*, pages 1–9, Madison, USA. American Society of Agronomy.
- Vega, A., Córdoba, M., Castro-Franco, M., and Balzarini, M. (2019). Protocol for automating error removal from yield maps. *Precision Agriculture*.
- Zhou, X., Helmers, M. J., Asbjornsen, H., Kolka, R., and Tomer, M. D. (2010). Perennial filter strips reduce nitrate levels in soil and shallow groundwater after grassland-to-cropland conversion. *Journal of Environment Quality*, 39(6):2006.

**APPENDIX**

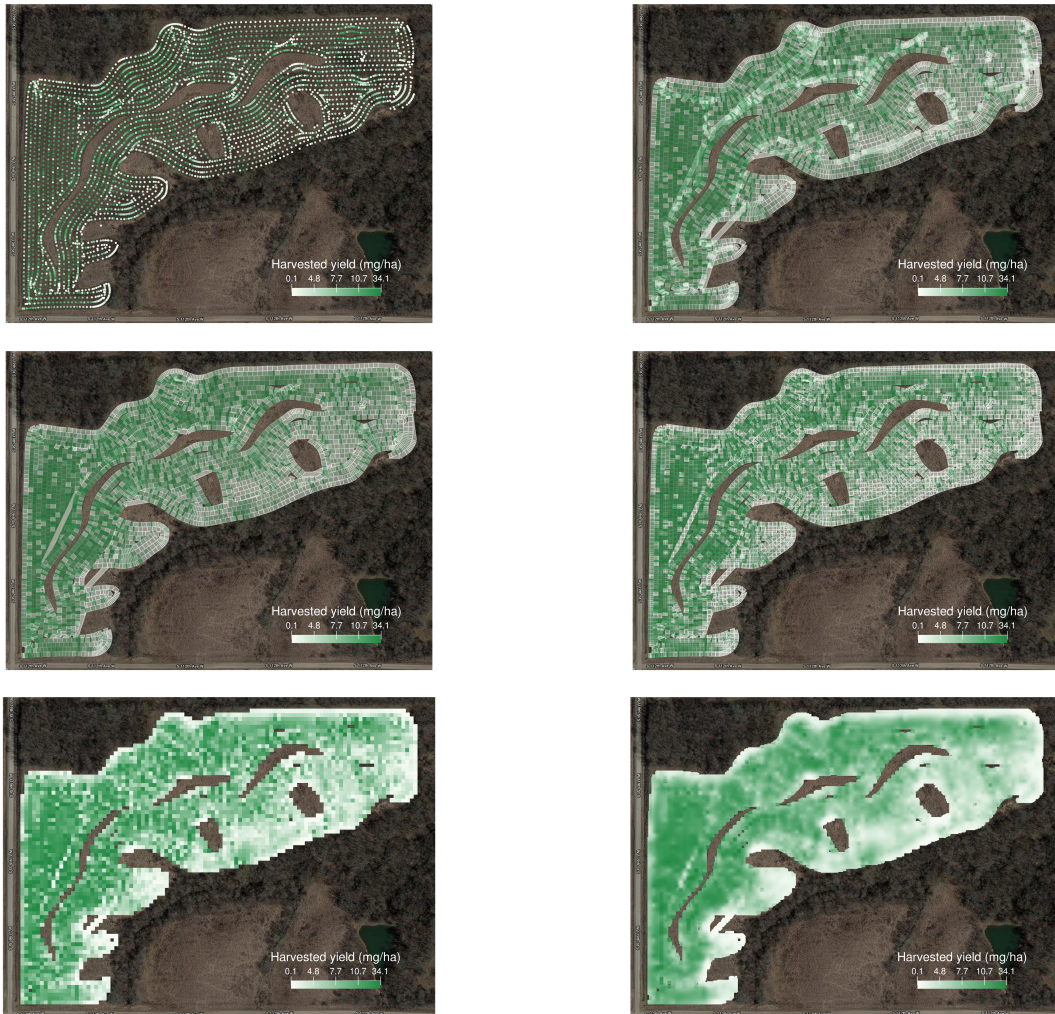


Figure .1 Every step progression. Point and intersection maps in the top row, reshaped and clipped maps in the middle row, and aggregated and smooth maps in the bottom row.